Temperature and strain rate dependence of microstructural evolution and dynamic mechanical behavior in nanocrystalline ti

Shixiong Zhang, Ying Chun Wang, Alexander P. Zhilyaev, Elena Korznikova, Shukui Li, Georgy I. Raab, Terence G. Langdon

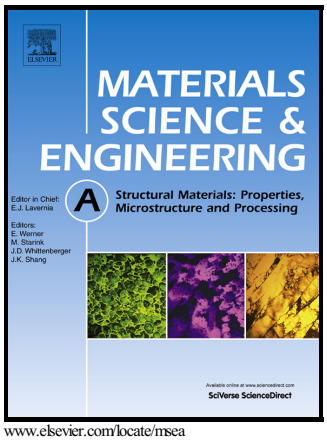

www.elsevier.com/locate/msea

PII: S0921-5093(15)30090-3
DOI: http://dx.doi.org/10.1016/j.msea.2015.06.035
Reference: MSA32473

To appear in: *Materials Science & Engineering A*

Received date: 18 March 2015
Revised date: 9 June 2015
Accepted date: 10 June 2015

Cite this article as: Shixiong Zhang, Ying Chun Wang, Alexander P. Zhilyaev, Elena Korznikova, Shukui Li, Georgy I. Raab and Terence G. Langdon, Temperature and strain rate dependence of microstructural evolution and dynamic mechanical behavior in nanocrystalline ti, *Materials Science & Engineering A,* http://dx.doi.org/10.1016/j.msea.2015.06.035

Submitted to Materials Science and Engineering A (June 2015)

Temperature and strain rate dependence of microstructural evolution and dynamic mechanical behavior in nanocrystalline Ti

Shixiong Zhang [a], Ying Chun Wang [a*], Alexander P. Zhilyaev [b,c], Elena Korznikova [b], Shukui Li [a], Georgy I. Raab [d], Terence G. Langdon [e]

[a] School of Materials Science and Engineering, Beijing Institute of Technology, Beijing 100081, China

[b] Institute for Problems of Metals Superplasticity, Russian Academy of Sciences, Khalturina 39, Ufa 450001, Russia

[c] Research Laboratory for Mechanics of New Nanomaterials, St. Petersburg State Polytechnical University, Polytechnicheskaya 29, St. Petersburg 195251, Russia

[d] Institute of Physics of Advanced Materials, Ufa State Aviation Technical University, 12 K. Marx Street, Ufa 450000, Russia

[e] Materials Research Group, Faculty of Engineering and the Environment, University of Southampton, Southampton SO17 1BJ, UK

*Corresponding author at: No 5 ZhongguanCun South Street, Haidian District, Beijing, China. Tel: +86-010-68913937 ext.801. Fax: +86-010-68913937 ext.808. E-mail: wangyc@bit.edu.cn (Y.C. Wang).

Abstract: The mechanical behavior of commercial purity titanium with a nanocrystalline (NC) grain size was investigated using split Hopkinson pressure bar tests at high strain rates and over a range of temperatures. The study was accompanied by detailed microstructural investigations before and after compression testing. The results show that rotary dynamic recrystallization operates during compressive deformation at strain rates of ~3000 and ~4500 s^{-1} at temperatures from 298 to 573 K but cells form at 673 K. The dynamic mechanical behavior of NC Ti shows a strong dependence on temperature and strain rate such that the flow stress and the strain hardening rate both increase with increasing strain and decreasing temperature. A constitutive equation is derived to relate the flow stress to the temperature, strain rate and true strain and to predict the yield strength and the peak stress of NC Ti subjected to dynamic deformation at elevated temperatures.

Keywords: dynamic compression; microstructure; mechanical behavior; constitutive equation; titanium

1. Introduction

Commercial purity titanium is widely used in the aerospace and biomedical fields due to its excellent mechanical and physical properties such as good ductility, excellent corrosion resistance and biological compatibility [1,2]. Nevertheless, the low strength of pure Ti tends to significantly reduce the potential applications. Through the introduction of severe plastic deformation (SPD) techniques, and combinations of SPD with other traditional deformation procedures, it is possible to fabricate ultrafine-grained (UFG) and nanocrystalline (NC) Ti which shows excellent properties including enhanced strength and good ductility [3-9]. Equal-channel angular pressing (ECAP) [10], one of the major SPD techniques, is especially attractive for fabricating relatively large volumes of homogeneously deformed bulk UFG/NC materials [11-15] and some reports suggest that a two-step processing route of ECAP combined with drawing [16-18], extrusion [19,20] or rolling [8,21] may be utilized successfully to even further improve the mechanical properties of UFG/NC Ti.

In practice, because of the overall features of many of its applications, pure Ti is frequently subjected to dynamic impact loading during the course of its service life, even under high temperature working conditions, and, as a result, it is subjected to high strain rates in elevated temperature deformation. In order to fully characterize titanium for potential applications under extreme conditions, it is necessary to examine the dynamic mechanical behavior and to clarify the microstructural evolution during dynamic deformation over a wide temperature range. Whilst there are many studies documenting the properties of UFG/NC Ti focusing on annealing instabilities [22], strain hardening behavior [23], tribological properties [24,25] and micro-hardness [26], relatively little attention has been

directed towards the effects of strain rate and temperature on the mechanical behavior and the microstructural evolution of UFG/NC Ti during dynamic impact deformation. Accordingly, this research was initiated to examine the dynamic mechanical properties and the microstructural evolution of NC Ti at high strain rates of ~10^3 s^{-1} over a range of temperatures. The fundamental emphasis of the research was to establish a constitutive relationship to predict the value of the flow stress under these extreme conditions. In addition, the dynamic mechanical properties are analyzed and compared directly with an earlier study where NC Ti was subjected to compression testing at a lower strain rate of 10 s^{-1} [27].

2. Experimental material and procedures

The experiments were conducted using commercial purity (CP) Ti of Grade 2 (ASTM B 348) with a chemical composition (in wt.%) of C 0.01; Fe 0.09; H 0.001; N 0.01; O 0.13 and with Ti as the balance. The material was processed at 473 K using ECAP-Conform [28,29] in which rods, having square sections of 14 × 14 mm^2, were constrained within a groove in a conventional conform facility and then forced to exit at an abutment where they were turned abruptly through an angle of 90° so that a strain of ~1 was introduced on each passage through the facility [30]. In the present experiments, the rods were processed for a total of 8 passes using processing route C in which the rods are rotated around their longitudinal axes by 180° between each pass [31]. Processing by ECAP-Conform was followed by drawing at 473 K to give rods with diameters of 6.3 mm.

Typical microstructures observed by transmission electron microscopy (TEM) and selected area electric diffraction (SAED) patterns are shown in Fig. 1 after ECAP and drawing for (a) a transverse section and (b) a longitudinal section. On the transverse section

in Fig. 1(a) there are uniform equiaxed grains with an average size of ~90 nm and the SAED pattern indicates a high fraction of high-angle grain boundaries (HAGBs). On the longitudinal section in Fig. 1(b) there are banded structures with elongated grains and sets of tangled dislocations and dislocation clusters distributed within the grain interiors.

For dynamic testing, cylindrical specimens with diameters of 5 mm and heights of 5 mm were cut from the two-step processed billets with the longitudinal axes oriented parallel to the axial directions of the cylinders. Dynamic compression was conducted using a split Hopkinson pressure bar (SHPB) at the two strain rates of ~3000 s^{-1} and ~4500 s^{-1} over a temperature range from 298 to 673 K. Elevated temperatures were obtained using a small furnace placed between the input and output bars of the SHPB setup. Before dynamic testing, each specimen was held at the test temperature for 10 min to ensure a homogeneous heat distribution throughout the sample. In order to separate the microstructure evaluation induced by high strain rate deformation during compressive testing from the thermal treatment prior to compression, a separate group of specimens was subjected to isothermal annealing for time of 10 min at temperatures of 473, 573 and 673 K.

The annealed and deformed specimens were cut along their longitudinal axes, prepared by mechanical grinding using grit papers with different particle sizes from 800 to 2000 mesh and then thinned to electron transparency using a Gatan Dual Ion Milling System. The prepared samples were examined with a JEM-2100 LaB_6 microscope operating at 100 kV for TEM investigations and for recording appropriate SAED patterns.

3. Experimental results

3.1 Microstructures after annealing

In order to evaluate the thermal stability of NC Ti, samples were heated to constant temperatures of 473, 573 and 673 K, respectively, held for 10 min at each temperature and then cooled in air. The TEM microstructures in the longitudinal sections and the corresponding SAED patterns are shown in Fig. 2 after annealing at each temperature. By comparing with Fig. 1(b), it is apparent from the microstructure and SAED pattern in Fig. 2(a) that no obvious transformation of grain size and shape occurs except that a much more clearly defined elongated structure is formed at 473 K. However, annealing at 573 K in Fig. 2(b) leads to elongated grains with diffuse boundaries and with recrystallized grains having a size of ~150 nm. The presence of diffuse boundaries was reported in early studies of materials subjected to SPD processing [32] and it is apparent from the SAED pattern in Fig. 2(b) that these new grain boundaries have high-angle misorientations.

Comparing Fig. 2(c) with Fig. 2(b), it can be seen that annealing at 673 K promotes both the formation of additional nano-sized grains and their subsequent growth. In Fig. 2(c), the structure generally evolves into polygons, the elongated grains transform to essentially equiaxed grains but the grain distribution is non-uniform. Thus, a few grains grow to sizes of ~700 nm while some grains have sizes of less than 150 nm. For this condition, the average grain size was measured as ~400 nm and the SAED pattern indicates the presence of a high fraction of HAGBs.

3.2 Microstructures after dynamic compression

Dynamic compressive deformation was conducted at ~3000 and ~4500 s^{-1} over a

temperature range from 298 to 673 K with the tests continued to fracture and the resultant microstructures and SAED patterns are displayed in Fig. 3. When NC Ti is compressed at 298 K with a strain rate of ~3000 s^{-1}, a large number of dislocations are generated and they propagate and tangle inside the elongated grains where the grain boundaries are visible but diffuse. In addition, some very small equiaxed grains of less than ~50 nm are also visible in Fig. 3(a) suggesting the occurrence of incomplete dynamic recrystallization (DRX). In Fig. 3(b) for the same strain rate at 473 K, the elongated grains develop into equiaxed grains via DRX to give an average grain size of ~190 nm. The grains formed during high strain rate deformation are nearly dislocation-free and the SAED patterns consist of rings of diffraction spots demonstrating the presence of boundaries having high angles of misorientation. Uniformly distributed equiaxed grains are visible in Fig. 3(c) after dynamic compression at the same strain rate at 573 K. For this condition, measurements gave an average grain size of ~80 nm which is smaller than the size of the grains after thermal treatment at the same temperature in Fig. 2(b) thereby confirming the occurrence of DRX induced by impact loading. In Fig. 3(d) after compression at ~3000 s^{-1} at 673 K, dislocation clusters and cells are observed inside the equiaxed grains which are formed during annealing in Fig. 2(c). The average grain size for this condition was measured as ~ 240 nm and the corresponding SAED pattern clear indicates small orientation differences between the cell structures which implies that the cells are formed when the dislocations abruptly multiply in high stain rate deformation.

The lower row of Fig. 3 shows similar observations for samples of NC Ti deformed at various temperatures at a strain rate of ~4500 s^{-1}. In Fig. 3(e) at 298 K, the original grain

boundaries achieved by the two-step processing are not visible and instead there are equiaxed grains with an average size of ~100 nm formed by the process of DRX. The corresponding SAED pattern suggests large misorientations between these recrystallized grains. At 473 K in Fig. 3(f), there are no well-defined grains and instead there is a polygonal structure consisting of dislocation clusters and networks. With increasing temperature to 573 K in Fig. 3(g), the equiaxed grains are visible again and they have grown to a coarser size of ~200 nm. The discontinuous rings in the SAED pattern implies the misorientations between these grains decreased by comparison with the microstructure in Fig. 3(c). Finally, in Fig. 3(h) at 673 K the microstructure is similar to Fig. 3(d) with a cell structure and an average size of ~200 nm.

These observations demonstrate that dynamic deformation at 3000 s^{-1} at temperatures of 298 to 573 K leads to the occurrence of DRX and this DRX becomes even more significant as the strain rate is increased to 4500 s^{-1} so that dislocations appear within the recrystallized grains. It is interesting to note also that both equiaxed grains and dislocation substructures are formed during dynamic compression and these are distributed very uniformly so that high strain rate deformation appears to be a favorable process for achieving a high level of microstructural homogeneity.

3.3 Significance of the flow stress

Fig. 4 illustrates the true stress-true strain curves of CP-Ti under dynamic compression at strain rates of ~3000 and ~4500 s^{-1} over a range of temperatures. It is readily apparent that the flow stress behavior is strongly influenced by the testing temperature so that, with an increase in temperature from 298 to 673 K, the flow stress decreases and the fracture strain

increases at both strain rates.

A comparison of Fig. 4(a) and (b) also provides information on the nature of the strain rate sensitivity of NC Ti. At the same testing temperature, the flow stress increases with increasing strain rate. Thus, at 298 K the yield strength ($\sigma_{0.2}$) is ~1570 MPa at a strain rate of ~3000 s^{-1} whereas it is ~1760 MPa at ~4500 s^{-1}. Nevertheless, when the temperature is increased from 298 to 673 K, the strain rate sensitivity of the flow stress is reduced. For example, at 673 K the value of $\sigma_{0.2}$ is ~1200 MPa at both strain rates of ~3000 and ~4500 s^{-1}. It should be noted that, based on earlier results [27], if the strain rate is increased from 10 s^{-1} to ~3000 s^{-1} then the flow stress increased even more. It is also apparent from Fig.4 that when the true stress reaches $\sigma_{0.2}$ there is a short period where the true stress increases quickly to the peak value and then gradually decreases suggesting that flow softening plays a significant role in further deformation.

4. Discussion

4.1 The recrystallization mechanism

It is generally considered that the static recrystallization (SRX) mechanism operating in deformation-induced UFG/NC metals during annealing is a continuous static recrystallization (c-SRX) [33,34] which may be classified into the three separate stages of recovery, transient recrystallization and normal grain growth [35]. In the present research, three stages were also present in NC Ti during the thermal treatment. Firstly, at 473 K static recovery occurs and produces no change in the grain size as shown in Fig. 2(a) but internal stresses are released due to the non-equilibrium nature of the grain boundaries and the presence of interior dislocation rearrangements. Thus, this stage may be considered as an incubation

period for the formation of new grains in the next stage. Secondly, SRX continues until completion at 573 K so that more new grains are formed until they impinge upon each other. Finally, conventional normal grain growth takes over in the third stage at 673 K with further annealing and the merging of larger grains with small grains.

The SRX operates during the thermal treatment at 573-673 K and this is significantly lower than the conventional recrystallization temperatures of 823-923 K for CP-Ti. It appears, therefore, that the intrinsic interfacial energy of the NC material is an important additional driving force which, in association with the deformation-stored energy and the added heat from the environment, facilitates the process of static recovery (SRV) and SRX during annealing. A similar result was also reported earlier where the grain size of UFG Ti was thermally stable at ~400 nm up to 723 K but SRX occurred at 773 K [22].

The dislocation-free grains presented in Fig. 3 indicate the occurrence of dynamic recrystallization (DRX) during dynamic compression testing and this was also reported during high strain rate deformation [36,37]. While SRX occurred at 473-573 K, the DRX initiated at a much lower temperature of 298 K. In practice, the recrystallization process may be assisted by the fast heat generation in the severe plastic deformation during impact testing. The magnitude of the adiabatic temperature rise, $\triangle T$, during high strain rate deformation was calculated in an earlier analysis [38]. During the deformation at ~3000 s^{-1} at 298 K, the instantaneous temperature of the sample increases to ~370 K and this is accompanied by the strain energy generated in high strain rate compression to stimulate the initiation of incomplete DRX as shown in Fig. 3(a). As the process is supported by increased values of $\triangle T$ at 473 and 573 K, together with deformation at the high strain rate,

DRX proceeds completely and leads to a homogeneous microstructure composed of dislocation-free nano-grains. At the higher strain rate of ~4500 s^{-1}, more adiabatic heat and strain energy are generated so that grain growth takes place and dislocation clusters emerge within the grains after DRX at 298~573 K.

A high strain rate will introduce a large strain in a very short time so that dislocations generate and multiply within the material in several hundred microseconds. With further deformation, these tangled high density dislocations evolve into cell structures and other dislocation substructures. Thus, these cell boundaries act as barriers to dislocation motion and gradually gain a grain boundary character by developing as subgrain boundaries with small misorientations. The orientation differences between the subgrains gradually increases so that the subgrain boundaries evolve into HAGBs in the process defined as DRX. In general, DRX is a phenomenon in which new grains with very few dislocations are developed homogeneously or inhomogeneously along initial grain boundaries through a nucleation and growth process [38]. The mechanism of DRX may be classified into migrational and rotational types [39] where it was reported that primarily migrational DRX operates in metals subjected to static deformation or low strain rate dynamic deformation [27,40,41]. Nevertheless, in deformation at very high strain rates, there is insufficient time for long-range migration of the boundaries so that the DRX operates via the rotation of subgrain boundaries [40,42].

The grain boundary rotation has been calculated in terms of grain boundary diffusion [43] and it was shown that grains having sizes of ~0.1-0.2 μm may be formed within an adiabatic shear band of a STS 316 stainless steel by rotational DRX (r-DRX) since grain

boundary diffusion is several times faster than the bulk diffusion at high deformation temperatures. In the present research, the initial NC Ti grain size after annealing at 473 and 573 K was no more than ~150 nm and the temperature rise due to the high strain rate deformation at the two experimental strain rates accelerated the grain boundary diffusion and thereby promoted the easy occurrence of r-DRX.

4.2 Dislocation cell formation

The r-DRX mechanism proceeds incompletely or completely when NC Ti is compressed at a high strain rate at temperatures of 298-573 K but at 673 K, although much adiabatic heat is generated during deformation, no DRX occurs because there are no equiaxed grain visible in Fig. 3(d) and (h). This is attributed to the process of recrystallization and grain growth which occurs during the annealing and consumes most of the stored energy to lead to an improved microstructural stability [44].

It is apparent that cells formed at the two strain rates show different sizes by comparing Fig. 3 (d) and (h) and this difference is explained by the following relationship [45]:

$$D = K\rho^{-1/2} \tag{2}$$

where D is the size of the dislocation cell, K is a constant related to the temperature and strain rate and ρ is the dislocation density. From Eq. (2) it follows that a higher strain rate will produce a higher dislocation density and therefore a smaller cell size. In addition, an increased strain rate introduces more dislocations and increases the propensity for the formation of dislocation intersections and tangles so that cell structures form more easily and tend to be smaller in size [46].

4.3 The strain hardening behavior

The strain hardening rate, Θ, defined as $\Theta = d\sigma/d\varepsilon$, is always employed to characterize the strain hardening behavior for a wide range of deformation conditions. From the flow curves in Fig. 4, it is obvious that the stress increases rapidly with strain at low strain levels and many dislocations are introduced during this early deformation resulting in a high value of the strain hardening rate in the initial deformation as shown in Fig. 5. Inspection shows that both Fig. 5(a) and (b) present a clear demonstration that the strain hardening rate decreases at a given true stress as the compressive temperature increases.

Moreover, the combined effect of changes in temperature and strain rate on the strain hardening rate may be considered and represented by a temperature-compensated strain rate using the Zener–Hollomon parameter Z defined as [47]

$$Z = \dot{\varepsilon} \exp\left(\frac{Q}{RT}\right) \tag{3}$$

where $\dot{\varepsilon}$ is the strain rate, Q is the activation energy of deformation, R is the gas constant and T is the absolute temperature.

It is easy to conclude from Eq. (3) that an increased strain rate and lower temperature leads to a higher value of Z. Accordingly, in order to clarify the relationship between Z and θ, three values of Z corresponding to three typical deformation conditions were selected. These were T = 298 K and $\dot{\varepsilon}$ = 3000 s^{-1}, T = 673 K and $\dot{\varepsilon}$ = 3000 s^{-1} and T = 298 K and $\dot{\varepsilon}$ = 4500 s^{-1} which were calculated as Z_l, Z_m and Z_h in terms of the value of the Z parameter. The curves of the strain hardening rate θ and Z versus strain are illustrated in Fig. 6 which shows that an increasing strain rate and decreasing temperature, corresponding to an increased value of Z, leads to an increase in θ.

This can be understood on the basis of the following relationship [48]:

$$\theta = \theta_0 - \frac{R}{\dot{\varepsilon}^{1/q}}\sigma \qquad (4)$$

where R and q are temperature dependent constants which are independent of stress and strain rate and θ_0 is a constant. It is clear that the strain hardening rate increases with increasing strain rate or decreasing temperature and this is because higher strain rates or lower temperatures provide shorter time for energy accumulation and reduced grain boundary mobility, thereby producing an increase in the strain hardening rate.

It is should be noted that θ does not always decrease with increasing temperature in Fig. 5(a) because θ at 673 K is higher than at either 473 or 573 K. In practice, the decline is closely related to the initiation of DRX during deformation. Thus, the recrystallized grains evolve from subgrains which are a consequence of the interaction of dislocations and subgrain boundaries and, as discussed elsewhere [49], some low-angle boundaries may act as sinks for dislocations. This means that dislocations disappear after the formation of new grains as shown in Fig. 3(b) and (c). It is intrinsically impossible to keep dislocations within these nanocrystalline grains due to image forces and interactions with grain boundaries and this suggests that dislocation pile-ups are not possible when the grain size is smaller than ~20 nm [50]. Thus, as new dislocation-free nano-grains are formed in the process of complete DRX, the new interfaces contribute to the strain hardening.

4.4 Establishment of Arrhenius-type constitutive equations

The stress–strain data obtained from the compression tests at elevated temperatures and different strain rates may be used to determine the material constants of the constitutive equation which is used to estimate the flow stress of a material during hot deformation. The effect of temperature and strain rate on the flow behavior is expressed by Eq. (3).

The Arrhenius-type constitutive equation is widely used to describe the relationship between the flow stress, strain rate and temperature. Three types of Arrhenius equations have been proposed and they are shown by the following [51,52]:

$$\dot{\varepsilon} = A_1 \sigma^{n_1} \exp\left(-\frac{Q}{RT}\right) \qquad \alpha\sigma < 0.8 \qquad (5)$$

$$\dot{\varepsilon} = A_2 \exp(\beta\sigma) \exp\left(-\frac{Q}{RT}\right) \qquad \alpha\sigma > 1.2 \qquad (6)$$

$$\dot{\varepsilon} = A[\sinh(\alpha\sigma)]^n \exp\left(-\frac{Q}{RT}\right) \qquad \text{for all } \sigma \qquad (7)$$

where Q is the deformation activation energy (in kJ mol^{-1}), A_1, A_2, A, n_1, n, α and β are material constants and $\alpha = \beta/n_1$.

For low stresses ($\alpha\sigma < 0.8$) and high stresses ($\alpha\sigma > 1.2$), it is possible to substitute a suitable function Aexp(-Q/RT) by B and take the logarithm of both sides to obtain

$$\ln \dot{\varepsilon} = n_1 \ln \sigma + \ln B_1 \qquad \text{for } \alpha\sigma < 0.8 \qquad (8)$$

and

$$\ln \dot{\varepsilon} = \beta\sigma + \ln B_2 \qquad \text{for } \alpha\sigma > 1 \qquad (9)$$

Generally, the peak value of the flow stress is adopted to establish the constitutive model. Thus, substituting the values of peak stresses and the corresponding strain rates at elevated temperatures where NC Ti was compressed at 3000 and 4500 s^{-1}, and using earlier results in Eqs. (8) and (9) where NC Ti was compressed at 10 s^{-1} [27] give the relationship between flow stress and strain rate as depicted in Fig. 7. Thus, it is obvious that the peak stresses obtained from the compression tests at 473, 573 and 673 K can be estimated by a group of straight and parallel lines and the values of n_1 and β are obtained from the slope of each line for a different temperature. Taking $\ln\dot{\varepsilon}$-lnσ and $\ln\dot{\varepsilon}$-σ plotted by linear fitting,

the average values of n_1 and β were computed as 15.423 and 0.0127 MPa^{-1}, respectively. The average linear correlation coefficient was also calculated as 0.9836 and 0.9870, respectively, as given in Fig. 7. The material constant α is defined as $\alpha = \beta/n_1 = 8.208\times10^4$ MPa^{-1}.

For all stress levels, Eq. (7) can be changed to the form

$$\ln\dot{\varepsilon} = n\ln[\sinh(\alpha\sigma)] + \ln A - \frac{Q}{RT} \qquad (10)$$

From Eq. (10), it is seen that at a constant temperature ln[sinh(ασ)] and $\ln\dot{\varepsilon}$ should show a linear relationship, and this is confirmed by the experimental results given in Fig. 8(a) for the peak stresses. The value of n is then obtained by making a linear fitting of $\ln\dot{\varepsilon}$ -ln[sinh(ασ)]. From the group of straight lines in Fig. 8(a), it is deduced that the average value of n is 11.537.

Differentiating Eq. (7) gives

$$Q = R\left\{\frac{\partial \ln\dot{\varepsilon}}{\partial \ln[\sinh(\alpha\sigma)]}\right\}_T \left\{\frac{\partial \ln[\sinh(\alpha\sigma)]}{\partial (1/T)}\right\}_{\dot{\varepsilon}} \qquad (11)$$

where

$$n = \left.\frac{\partial \ln\dot{\varepsilon}}{\partial \ln[\sinh(\alpha\sigma)]}\right|_T \qquad (12)$$

Therefore, by substituting the values of temperatures and peak stresses obtained at a fixed strain rate into Eq. (11), the value of Q may be derived from the slope of a plot of ln[sinh(ασ)] as a function of 1/T, as shown in Fig. 8(b). Since the slopes of these lines have approximately the same tendency, the average slope may be used to derive a value for the activation energy, Q, of ~285 kJ mol^{-1}. The value of lnA in Eq. (10) can be derived from the intercept of the linear fitting of $\ln\dot{\varepsilon}$ -ln[sinh(ασ)] and the value is estimated as ~5.6×10^4 s^{-1}.

The value of Q for coarse-grained pure Ti was reported as 218–240 kJ mol^{-1} [53] which is lower than in the present research. Thus, it appears that the activation energy may increase as the grains are refined. This is consistent with earlier research indicating that UFG Ti shows a relatively high value of Q of ~323-344 kJ mol^{-1}[54].

It follows, therefore, that the constitutive equation established to describe the peak stress of NC Ti deformed at constant strain rates ranging from10 to 4500 $s^{-1}$and at temperatures varying from 473 to 673 K can be expressed as

$$\dot{\varepsilon} = 5.6\times 10^{4}[\sinh(8.42\times 10^{-5}\sigma)]^{11} \exp\left(-\frac{2.86\times 10^{5}}{RT}\right) \qquad (13)$$

The constitutive equation for $\sigma_{0.2}$ was also inferred from the experimental data in the same way and leads to the following relationship:

$$\dot{\varepsilon} = 6.4\times 10^{5}[\sinh(7.7\times 10^{-4}\sigma)]^{11.5} \exp\left(-\frac{3.10\times 10^{5}}{RT}\right) \qquad (14)$$

5. Summary and conclusions

1. Experiments were conducted on commercial purity Ti to examine the effect of temperature and strain rate on the microstructural evolution and compressive behavior over a range of temperatures and dynamic strain rates after processing to produce a nanostructured condition using a two-step procedure of ECAP-Conform and drawing.

2. Continuous static recrystallization (c-SRX) was motivated by the high stored energy and high interfacial energy in nanocrystalline Ti including the three stages of recovery, transient recrystallization and normal grain growth. Rotary dynamic recrystallization (r-DRX) was promoted by the high strain rate deformation accompanied by an adiabatic temperature rise during dynamic compression at temperatures from 298 to 573 K at strain

rates of both ~3000 and ~4500 s^{-1}.

3. The formation of cells at these strain rates at 673 K was attributed to the energy consumed by SRX and grain growth during annealing, thereby leading to an enhancement in microstructural stability. The dynamic compressive behavior of nanocrystalline Ti was sensitive to the strain rate and temperature, such that the flow stress and strain hardening rate increased with increasing strain rate or decreasing temperature and the fracture strain increased with strain rate and temperature.

4. A constitutive Arrhenius-type relationship was derived from these results to formally define the flow stress and the peak stress.

Acknowledgements

This work was supported in part by the National Natural Science Foundation of China under Grant No.11221202, in part by the European Research Council under ERC Grant Agreement No. 267464-SPDMETALS and in part by the Russian Scientific Foundation under Grant No. 14-29-00199. The dynamic compression properties were obtained using a split Hopkinson pressure bar facility which is sponsored at the National Key Laboratory of Science and Technology on Materials under Shock and Impact and the State Key Laboratory of Explosion Science and Technology.

References

[1] G.Z. Luo, R.Z. Liu, Mater. Sci. Eng. A280 (2000) 25-29.

[2] S. Ferraris, A. Venturello, M. Miola, A. Cochis, L. Rimondini, S. Spriano, Appl. Surf. Sci. 311 (2014) 279-291.

[3] V.V. Stolyarov, Y.T. Zhu, T.C. Lowe, R.K. Islamgaliev, R.Z. Valiev, NanoStruct. Mater. 11

(1999) 947-954.

[4] R.K. Islamgaliev, V.U. Kazyhanov, L.O. Shestakova, A.V. Sharafutdinov, R.Z. Valiev, Mater. Sci. Eng. A493 (2008) 190-194.

[5] Z.G. Fan, H.Jiang, X.G. Sun, J. Song, X.N. Zhang, C.Y. Xie, Mater. Sci. Eng. A527 (2009) 45-51.

[6] W.J. Kim, S.J. Yoo, J.B. Lee, Scripta Mater. 62 (2010) 451-454.

[7] Y. Zhang, R.B. Figueiredo, S.N. Alhajeri, J.T. Wang, N. Gao, T.G. Langdon, Mater. Sci. Eng. A528 (2011) 7708-7714.

[8] V.L. Sordi, M. Ferrante, M. Kawasaki, T.G. Langdon, J. Mater. Sci. 47 (2012) 7870-7876.

[9] H.S. Liu, W. Pantleon, L. Mishnaevsky, Comp. Mater. Sci. 83 (2014) 318-330.

[10] R.Z. Valiev, T.G. Langdon, Prog. Mater. Sci. 51 (2006) 881-981

[11] J. Gubicza, N.Q. Chinh, P. Szommer, A. Vinogradov, T.G. Langdon, Scripta Mater. 56 (2007) 947-950.

[12] M. Reihanian, R. Ebrahimi, N. Tsuji, M.M. Moshksar, Mater. Sci. Eng. A473 (2008) 189-194.

[13] J. Gubicza, N.Q. Chinh, J.L. Lábár, S. Dobatkin, Z. Hegedüs, T.G. Langdon, J. Alloys Compds 483 (2009) 271-274.

[14] Y.J. Chen, Y.J. Li, J.C. Walmsley, S. Dumoulin, P.C. Skaret, H.J. Roven, Mater. Sci. Eng. A527 (2010) 789-796.

[15] N.D. Stepanov, A.V. Kuznetsov, G.A. Salishchev, G.I. Raab, R.Z. Valiev, Mater. Sci. Eng. A554 (2012) 105-115.

[16] I. Sabirov, M.T. Perez-Prado, J.M. Molina-Aldareguia, I.P. Semenova, G.Kh. Salimgareeva, R.Z. Valiev, Scripta Mater. 64 (2011) 69-72.

[17] D.V. Gunderov, A.V. Polyakov, I.P. Semenova, G.I.Raab, A.A. Churakova, E.I. Gimaltdinova, I. Sabirov, J. Segurado, V.D. Sitdikov, I.V. Alexandrov, N.A. Enikeev, R.Z.Valiev, Mater. Sci. Eng. A562 (2013) 128-136.

[18] A.V. Polyakov, I.P. Semenova, R.Z. Valiev, Y. Huang, T.G. Langdon, MRS Comm. 3 (2013) 249-253.

[19] V.V. Stolyarov, Y.T. Zhu, T.C. Lowe, R.Z. Valiev, Mater. Sci. Eng. A303 (2001) 82 -89.

[20] A.V. Polyakov, I.P. Semenova, Y. Huang, R.Z. Valiev, T.G. Langdon, Adv. Eng. Mater. 16 (2014) 1038-1043.

[21] V.V. Stolyarov, Y.T. Zhu, I.V. Alexandrov, T.C. Lowe, R.Z. Valiev, Mater. Sci. Eng. A343 (2003) 43-50.

[22] M. Hoseini, M. H. Pourian, F. Bridier, H. Vali, J.A. Szpunar, P. Bocher, Mater. Sci. Eng. A532 (2012) 58-63.

[23] Y. G. Ko, D. H. Shin, K.T. Park, C.S. Lee, Scripta Mater. 54 (2006) 1785-1789.

[24] P.Q. La, J.Q. Ma, Y.T. Zhu, J. Yang, W.M. Liu, Q.J. Xue, R.Z. Valiev, Acta Mater. 53 (2005) 5167-5173.

[25] C.T. Wang, N. Gao, M.G. Gee, R.J.K. Wood, T.G. Langdon, Wear 280- 281 (2012) 28-35.

[26] K.P. Sanosh, A. Balakrishnan, L. Francis, T.N. Kim, J. Mater. Sci. Technol. 26 (2010) 904-907.

[27] S.X. Zhang, Y.C. Wang, A.P. Zhilyaev, D.V. Gunderov, S.K. Li, G..I. Raab, E. Korznikova, T.G. Langdon, Mater. Sci. Eng. A634, (2015) 64-70.

[28] G.J. Raab, R.Z. Valiev, T.C. Lowe, Y.T. Zhu, Mater. Sci. Eng. A382 (2004) 30-34.

[29] C. Xu, S. Schroeder, P.R. Berbon, T.G. Langdon, Acta Mater. 58 (2010) 1379-1386.

[30] Y. Iwahashi, J. Wang, Z. Horita, M. Nemoto, T.G. Langdon, Scripta Mater. 35 (1996) 143-146.

[31] M. Furukawa, Y. Iwahashi, Z, Horita, M. Nemoto, T.G. Langdon, Mater. Sci. Eng. A257 (1998) 328-332.

[32] J. Wang, Z. Horita, M. Furukawa, M. Nemoto, N.K. Tsenev, R.Z. Valiev, Y. Ma, T.G. Langdon, J. Mater. Res. 8 (1993) 2810-2818.

[33] H. Jazaeri, F.J. Humphreys, Acta Mater. 52 (2004) 3251-3262.

[34] A. Belyakov, T. Sakai, H. Miura, R. Kaibyshev, K. Tsuzaki, Acta Mater. 50 (2002) 1547-1557.

[35] A. Takayama, X. Yang, H. Miura, T. Sakai, Mater. Sci. Eng. A478 (2008) 221-228.

[36] L. Wang, Y.C. Wang, A.P. Zhilyaev, A.V. Korznikov, S.K. Li, E. Korznikova, T.G. Langdon, Scripta Mater. 77 (2014) 33-36.

[37] G. Dirrasa,, H. Couque, J. Gubicza, A. Ouarem, T. Chauveau, P. Jenei, Mater. Sci. Eng. A527 (2010) 4128-4135.

[38] L. Wang, Y.C. Wang, A.P. Zhilyaev, A.V. Korznikov, S.K. Li, E. Korznikova, T.G. Langdon, J. Mater. Sci. 19 (2014) 6640-6647.

[39] B. Derby, Acta Metall. Mater. 39 (1991) 955-962.

[40] S. Wu, K. Fan, P. Jiang, S. Chen, Mater. Sci. Eng. A527 (2010) 6917-6921.

[41] A.Samet-Meziou, A.L. Helbert-Etter, T. Baudin, Mater. Sci. Eng. A528 (2011) 3829-3832.

[42] B. Hwang, S. Lee, Y.C. Kim, N.J. Kim, D.H. Shin, Mater. Sci. Eng. A441 (2006) 308-320.

[43] M.A. Meyers, Y.B. Xu, Q. Xue, M.T. Perez-Prado, T.R. McNelley, Acta Mater. 51 (2003) 1307-1325..

[44] C.F. Gu, C.H.J. Davies, Mater. Sci. Eng. A527 (2010) 1791-1799.

[45] N.A. Koneva, V.A. Starenchenko, D.V. Lychagin, L.I. Trishkina, N.A. Popova, E.V. Kozlov, Mater. Sci. Eng. A483-484 (2008) 179-183.

[46] H.J. Ma, L. Huang, Y. Tian, J.J. Li, Mater. Sci. Eng. A606 (2014) 233-239.

[47] M.H. Wang, Y.F. Li, W.H. Wang, J. Zhou, A. Chiba, Mater. Des. 45 (2013) 384-392.

[48] U.F. Kocks., H. Mecking, Prog. Mater. Sci. 48 (2003) 171-273.

[49] J. May, H.W. Höppel, M. Göken, Scripta Mater. 53 (2005) 189-194.

[50] Y.M. Wang, E. Ma, Acta Mater. 52 (2004) 1699-1709.

[51] Y.C. Lin, X.M. Chen, Mater. Des. 32 (2011) 1733-1759.

[52] C.M. Sellars, W.J.McG. Tegart, Mem. Sci. Rev. Metall. 63 (1966) 731-746.

[53] Z.P. Zeng, S. Jonsson, Y.S. Zhang, Mater. Sci. Eng. A505 (2009) 116-119.

[54] S.V. Sajadifar, G.G. Yapici, Mater. Des. 53 (2014) 749-757.

Figure

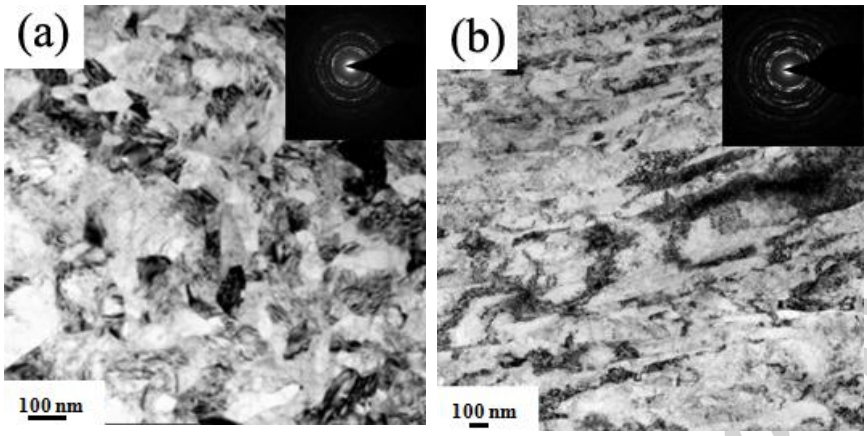

Figure 1. TEM images and SAED patterns of a CP-Ti billet processed by ECAP-Conform and then drawing (a) in a transverse section and (b) in a longitudinal section.

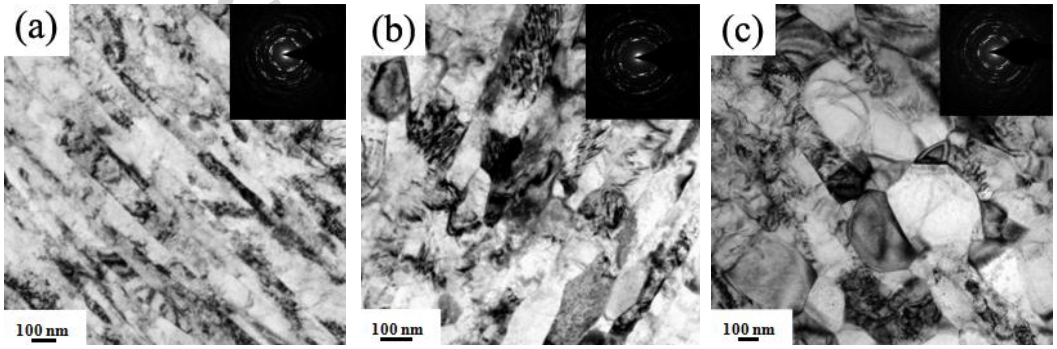

Figure 2. TEM microstructures and SAED micrographs in the longitudinal sections of specimens annealed for 10 min at (a) 473 K, (b) 573 K and (c) 673 K.

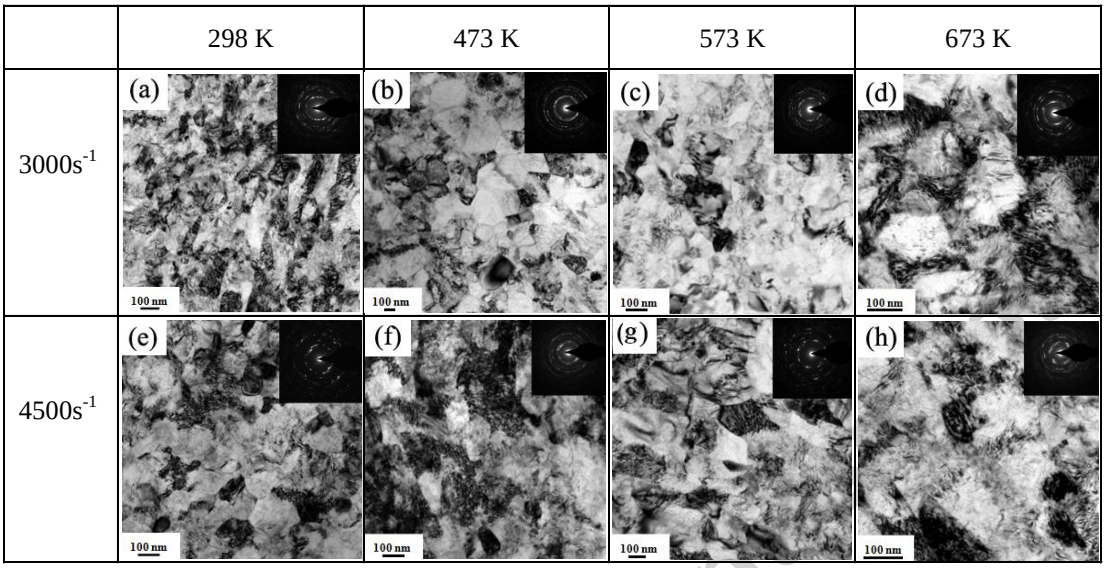

Figure 3. TEM microstructures and SAED micrographs in the longitudinal sections of specimens deformed under high strain rate compression at various temperatures.

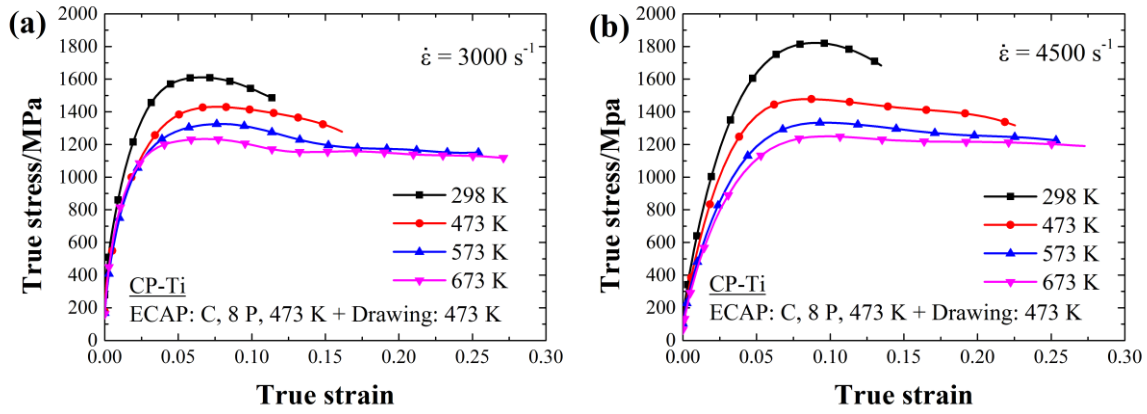

Figure 4. True stress-true strain curves of NC Ti deformed at different deformation temperatures at strain rates of (a) 3000 s^{-1} and (b) 4500 s^{-1}

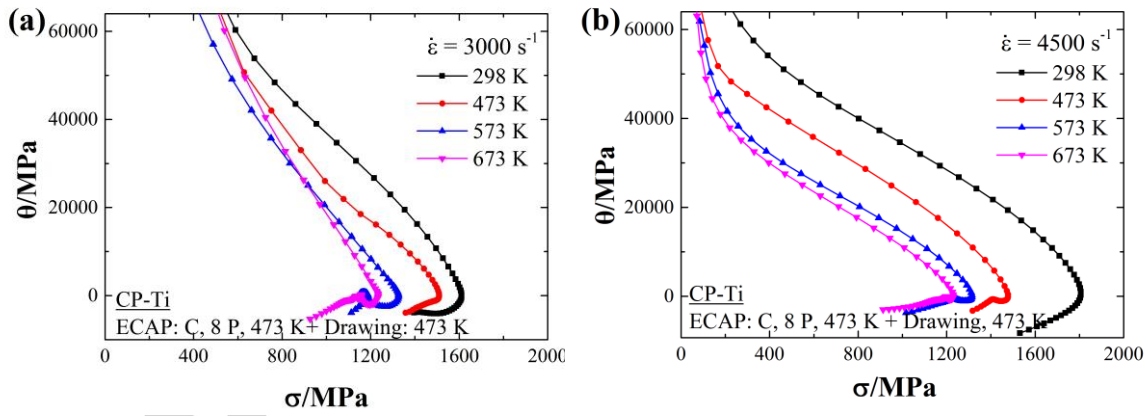

Figure 5. Strain hardening rate vs. true stress at different deformation temperatures with strain rates of (a) 3000 s^{-1} and (b) 4500 s^{-1}

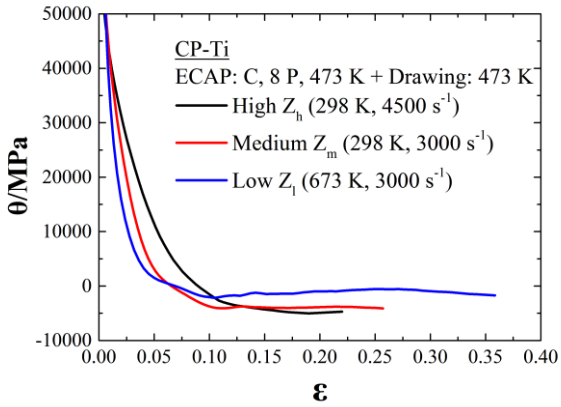

Figure 6. Variation of strain hardening rate with true strain at high, medium and low Z values.

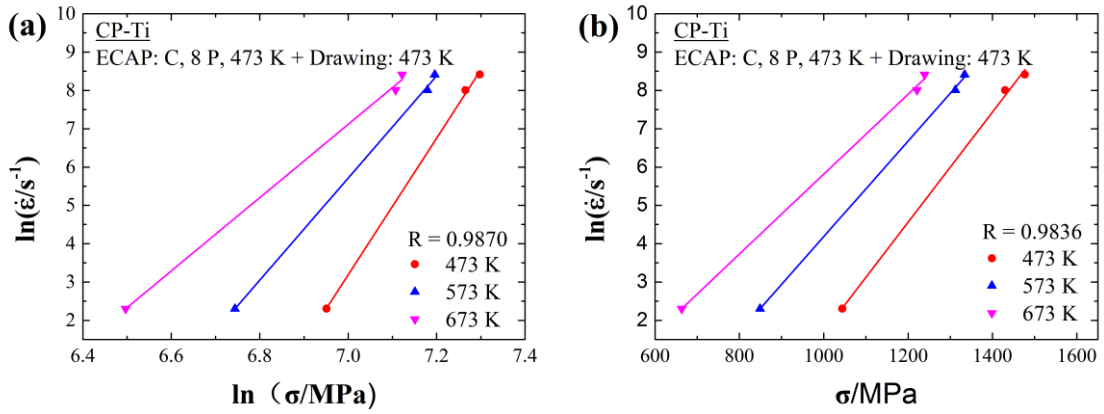

Figure 7. Evaluating the value of (a) n_1 by fitting $\ln\dot{\varepsilon}$ -lnσ and (b) β by fitting $\ln\dot{\varepsilon}$ -σ.

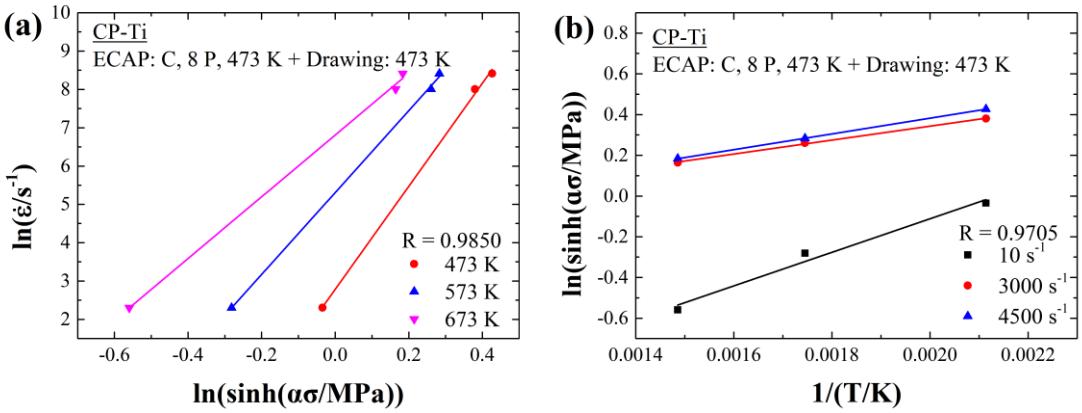

Figure 8. Evaluating the value of (a) n by fitting $\ln \dot{\varepsilon}$ -ln[sinh(ασ)] and (b) Q by fitting ln[sinh(ασ)]-1/T.